

# THE UNIVERSITY OF WARWICK

**Original citation:**

Yin, D.D., Wang, Q.D., Boehlert, C.J., Janik, V. (2012). Creep and Fracture Behavior of Peak-Aged Mg-11Y-5Gd-2Zn-0.5Zr (wt pct). Metallurgical and Materials Transactions A, 43(9) pp. 3338-3350

**Permanent WRAP url:**

<http://wrap.warwick.ac.uk/48620>

**Copyright and reuse:**

The Warwick Research Archive Portal (WRAP) makes the work of researchers of the University of Warwick available open access under the following conditions. Copyright © and all moral rights to the version of the paper presented here belong to the individual author(s) and/or other copyright owners. To the extent reasonable and practicable the material made available in WRAP has been checked for eligibility before being made available.

Copies of full items can be used for personal research or study, educational, or not-for-profit purposes without prior permission or charge. Provided that the authors, title and full bibliographic details are credited, a hyperlink and/or URL is given for the original metadata page and the content is not changed in any way.

**Publisher's statement:**

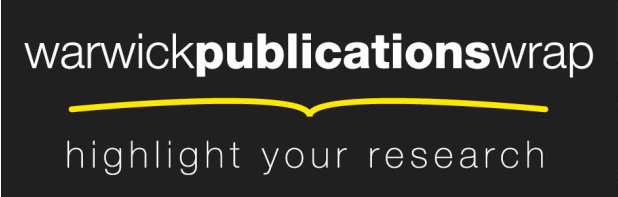
The original publication is available at [www.springerlink.com](http://www.springerlink.com)

DOI: 10.1007/s11661-012-1131-7

**A note on versions:**

The version presented here may differ from the published version or, version of record, if you wish to cite this item you are advised to consult the publisher's version. Please see the 'permanent WRAP url' above for details on accessing the published version and note that access may require a subscription.

For more information, please contact the WRAP Team at: [wrap@warwick.ac.uk](mailto:wrap@warwick.ac.uk)



warwick**publications**wrap  
highlight your research

<http://go.warwick.ac.uk/lib-publications>

# Creep and rupture behavior of peak-aged Mg-11Y-5Gd-2Zn-0.5Zr (wt.%)

D.D. Yin <sup>a</sup>, Q.D. Wang <sup>a, b, \*</sup>, C.J. Boehlert <sup>c</sup>, V. Janik <sup>a, d</sup>

<sup>a</sup> National Engineering Research Center of Light Alloy Net Forming, School of Materials Science and Engineering, Shanghai Jiao Tong University, 800 Dongchuan Road, Shanghai 200240, P.R. China

<sup>b</sup> The State Key Laboratory of Metal Matrix Composites, School of Materials Science and Engineering, Shanghai Jiao Tong University, 800 Dongchuan Road, Shanghai 200240, P.R. China

<sup>c</sup> Department of Chemical Engineering and Materials Science, Michigan State University, East Lansing, Michigan, 48824, USA

<sup>d</sup> Czech Technical University in Prague, Karlovo nam. 13, Prague 12135, Czech Republic

---

\* Corresponding author: National Engineering Research Center of Light Alloys Net Forming and State Key Laboratory of Metal Matrix Composites, School of Materials Science and Engineering, Shanghai Jiao Tong University, 800 Dongchuan Road, 200240 Shanghai, PR China. Tel.: +86-21-54742715; Fax: +86-21-34202794.

E-mail address: [wangqudong@sjtu.edu.cn](mailto:wangqudong@sjtu.edu.cn) (Q.D. Wang).

**Abstract:** The tensile-creep and creep-rupture behavior of heat-resistant peak-aged Mg-11Y-5Gd-2Zn-0.5Zr (wt.%) (WGZ1152) was investigated at  $T=523-598\text{K}$  ( $0.58-0.66T_m$ ) and stresses between 30MPa to 140MPa. The minimum creep rate of the alloy was almost two orders of magnitude lower than that for WE54-T6, and was comparable to that for HZ32-T5. The creep behavior exhibited an extended tertiary creep stage, which was believed to be associated with precipitate coarsening. The creep stress exponent value was 4.5, suggesting that dislocation creep was the rate-controlling mechanism. The activation energy for creep ( $221 \pm 20\text{kJ/mol}$ ) was higher than that for self-diffusion in magnesium, and was believed to be associated with the activation of non-basal slip and cross slip. This was consistent with the surface deformation observations, which revealed a transition from basal slip to non-basal slip and cross slip with increasing temperature. The minimum creep rate and rupture time followed the original and modified Monkman-Grant relationships. The microcracks and cavities preferentially nucleated at grain boundaries and at the interface between Mg matrix and the second phase. *In-situ* creep experiments highlighted the intergranular cracking evolution.

**Keywords:** Mg-RE alloy; Creep rupture; Monkman-Grant relationship; Creep damage tolerance parameter; *in-situ*; Slip trace

## 1. Introduction

In the last decade research and development of high-performance creep resistant magnesium (Mg) alloys for elevated-temperature applications has drawn considerable attention.<sup>[1-4]</sup> In addition to the aerospace industry, Mg alloys have made significant progress in the automotive industry where weight and fuel economy are important considerations.<sup>[1,3]</sup> Most commercially used Mg alloys for automotive applications are Mg-Al based alloys, such as AZ (Mg-Al-Zn) series and AM (Mg-Al-Mn) series, and they can't be used for major powertrain applications due to their poor creep resistance at temperatures above 398K.<sup>[4,5]</sup> These powertrain applications work at

higher temperatures. For instance, automatic transmission cases can operate at up to 448K, engine blocks up to 473K, and engine pistons up to 573K.<sup>[4]</sup> Creep resistance is a major requirement for Mg alloys in automotive powertrain applications, for which aluminum or cast iron are typically used.<sup>[4]</sup> Consequently, efforts are being focused on developing Mg alloys with sufficient creep resistance at temperatures up to 573K, depending on the application.<sup>[6]</sup>

The addition of rare earth (RE) elements to Mg alloy can lead to increased creep resistance at temperatures up to 573K.<sup>[1-3,6,7]</sup> Rare earths can be divided into two groups: Y group (Y, Gd-Lu) and Ce group (La-Eu).<sup>[1,6,7]</sup> The Y group has higher solid solution strengthening and precipitation hardening.<sup>[1,6,7]</sup> Recently, a Mg-Y based alloy, Mg-11Y-5Gd-2Zn-0.5Zr (wt.%) (WGZ1152), has been developed which exhibits excellent elevated-temperature mechanical properties, making it promising for engine piston applications.<sup>[8-10]</sup> Our previous work has focused on its microstructure, thermal properties, tensile strength and fatigue strength.<sup>[8-11]</sup> However, little is known about this alloy's creep and rupture behavior. The aim of the present work was to investigate the creep and rupture behavior of peak-aged WGZ1152 at 523-598K (0.58-0.66 $T_m$ ) and stresses between 30MPa to 140MPa.  $T_m$  is the absolute melting temperature of the studied alloy, which is approximately 901K.<sup>[9]</sup> The microstructural evolution, creep deformation, and rupture behavior relationship are discussed.

## 2. Experimental procedures

The measured composition of the studied alloy, measured using an inductively coupled plasma (ICP) analyzer, was Mg-11.3Y-4.7Gd-2.0Zn-0.46Zr (wt.%). It was prepared from high-purity ( $\geq 99.9\%$ ) Mg, Zn, Mg-25Y (wt.%), Mg-25Gd (wt.%) and Mg-30Zr (wt.%) master alloys by electronic resistance melting in a mild steel crucible at approximately 1023K under a mixed atmosphere of CO<sub>2</sub> and SF<sub>6</sub>. The ratio of CO<sub>2</sub> gas to SF<sub>6</sub> gas was 100:1. The alloy was cast into a steel mold pre-heated to 473K. The peak-aged T6 heat-treatment, described in our previous

study,<sup>[9]</sup> was performed at 808K for 20 hours followed by water quenching then aging at 498K for 24 hours in an oil bath furnace. The WE54 ingot [Mg-5.2Y-3.6RE-0.5Zr (wt.%)] for comparison tests was bought from a commercial company, and was subjected to the following heat treatment: solution treatment of 8h at 798K, a hot water quench and a subsequent aging treatment of 16h at 523K.<sup>[1]</sup>

Conventional tensile creep tests were performed at 523-598K under constant load in air. Rectangular tensile creep specimens, 6mm in width, 2mm in thickness, and 25mm in gage length, were cut from the ingot by an electric discharge machine (EDM). In order to achieve thermal stability, the specimens were held at the test temperature for 1 hour before loading. The temperature was maintained constant within  $\pm 1\text{K}$  of the target temperature along the entire gage length. The strain was measured using a calibrated linear variable differential transformer, which was attached to the gauge section of the specimens, and all temperature-stress-strain-time data were collected by a computer-controlled data acquisition system. Most of the specimens were taken to failure. Some of the specimens were interrupted after 1000 hours or longer. Some creep tests were repeated, and similar results were found for the two duplicate specimens. The data of the duplicate specimens were listed below. At  $T=573\text{K}$  ( $T$ =absolute temperature) and  $\sigma=30\text{MPa}$  ( $\sigma$ =stress), the minimum creep rates for the duplicate specimens were  $1.68\text{E-}9$  and  $1.46\text{E-}9 \text{ S}^{-1}$ , respectively. At  $T=573\text{K}$  and  $\sigma=50\text{MPa}$ , the minimum creep rates for the duplicate specimens were  $6.74\text{E-}9$  and  $7.28\text{E-}9 \text{ S}^{-1}$ , respectively. At  $T=573\text{K}$  and  $\sigma=80\text{MPa}$ , the minimum creep rates for the duplicate specimens were  $1.07\text{E-}7$  and  $1.27\text{E-}7 \text{ S}^{-1}$ , respectively. Unless “*in-situ*” was noted otherwise, the data used for the creep analysis were from the conventional tensile creep tests, and were the average data if the tests were repeated.

*In-situ* tensile-creep experiments were conducted. Flat dogbone-shaped samples, with gage dimensions of 3mm wide by 2.5mm thick by 10mm long, were EDM cut. The specimens were

glued to a metallic platen and polished to a 1 $\mu$ m finish using an automatic polishing machine and ethanol as a polishing lubricant. These experiments were performed using a screw-driven tensile stage placed inside a Zeiss (Jena, Germany) EVO MA15 SEM. Temperature was controlled using a constant-voltage power supply to a 6mm diameter tungsten-based heater located just below the gage section of the sample. An open-bath, closed-loop chiller was used to circulate distilled water at RT through copper tubes to prevent the tensile stage from overheating. A fine-gage K-type thermocouple was spot-welded to the gage section of each sample. After the sample's gage-section temperature reached the desired creep temperature, a 30 minute period was given to stabilize the thermal stress prior to applying load. The load, which was measured using a 4,448 N load cell, was applied at 5N/s until reaching the desired creep stress. The tests were considered constant load where the stress fluctuation varied  $\pm 3$ MPa. The displacement data acquired during the experiments comprised that of the sample as well as the gripping fixtures. Thus, the displacement values reported do not represent the sole displacement of the reduced gage section of the sample. Secondary electron (SE) SEM images were taken before loading and at periodic displacements throughout the creep experiments without interrupting the experiment. The pressure in the SEM chamber never exceeded  $10^{-6}$  torr, and therefore oxidation did not detrimentally affect the SEM imaging. Further details of this apparatus and testing technique can be found elsewhere.<sup>[12,13]</sup>

Microstructural observations, both prior to and after deformation, were made using optical microscopy (LEICA MEF4M), scanning electron microscopy (FEI SIRION 200 and Camscan 44FE), and transmission electron microscopy (JEM-2010). The specimens for surface observations of *ex-situ* experiments were mechanical polished, and then etched in a 4 vol.% nital. After the etch, the specimens were creep tested to the desired creep stage, using the same machine used for the conventional creep experiments, and then water quenched under load. The slip traces

analysis were performed after the *in-situ* creep test at  $T=573\text{K}$  and  $\sigma=50\text{MPa}$  by SE SEM and electron backscatter diffraction (EBSD). The active slip systems were identified from the SE SEM images and the EBSD orientation data using a MATLAB code with the inputs of grain Euler angles and all available slip systems. Sample preparation for EBSD was mechanically polished and chemically etched in a solution of 5 ml nitric acid, 15 ml acetic acid, 20 ml water and 60 ml ethanol for 1-2 s. A step size of 1.5 or 3  $\mu\text{m}$  was used to collect the EBSD data using a TSL OIM EBSD system fitted to a Camscan 44FE SEM.

### 3. Results

#### 3.1 Creep deformation

Fig. 1-3 illustrate creep strain rate versus time and creep strain rate versus creep strain curves of WGZ1152-T6 specimens at  $T=523\text{-}598\text{K}$  and  $\sigma=30\text{-}140\text{MPa}$ . Note that the specimens which were creep tested to failure were indicated with “X”. The creep resistance decreased with increasing stress and temperature. There was not a well-defined steady-state creep regime, especially at high temperatures and low stresses. For instance, the tertiary creep started at approximately  $0.1t_r$  (8h) for  $T=598\text{K}$  and  $\sigma=50\text{MPa}$ , and at approximately  $0.3t_r$  (12h) for  $T=573\text{K}$  and  $\sigma=80\text{MPa}$ . Where  $t_r$  is rupture time. After a normal primary stage in which the creep strain rate decreased with increasing time and creep strain, the creep strain rate reached its minimum, and then increased slowly with increasing time and creep strain. This creep behavior is usually called as “tertiary-dominated creep”<sup>[14]</sup> or “extended tertiary creep”<sup>[15,16]</sup>. In the tertiary creep regime, the creep strain rate increased with increasing time and creep strain until rupture occurred.

Fig. 4 shows the log-log plot of the stress dependence on the minimum creep rate at  $T=523\text{-}598\text{K}$ . Note that the data of WE54-T6 and HZ32<sup>[5]</sup> [Mg-3.3Th-2.1Zn-0.7Zr (wt.)]-T5

were also included for comparison. WE54 is the most commercially used structural Mg alloys for elevated-temperature applications up to 523K,<sup>[2,17,18]</sup> and HZ32 is the Mg alloy which has been used at the highest service temperatures ( $618 \leq T \leq 643\text{K}$ ).<sup>[2,6]</sup> However, HZ32 is being phased out due to its radioactivity.<sup>[6,18]</sup> The peak-aged WGZ1152-T6 exhibited superior creep resistance compared to the WE54-T6 at  $T=523\text{-}573\text{K}$  ( $0.58\text{-}0.64T_m$ ) and  $\sigma=50\text{-}80\text{MPa}$ , and was comparable to the HZ32-T5 at  $T=573\text{K}$  and  $\sigma=30\text{MPa}$ . At  $T=573\text{K}$  and  $\sigma=50\text{MPa}$ , the minimum creep rate of the WGZ1152-T6 was almost two orders of magnitude lower than that for WE54-T6, and the creep rupture life of WGZ1152-T6 (676h) was more than ten times longer than that for WE54-T6 (53h). At  $T=573\text{K}$  and  $\sigma=80\text{MPa}$ , the minimum creep rate of the WGZ1152-T6 was more than one order of magnitude lower than that for WE54-T6, and the creep rupture life of WGZ1152-T6 (41h) was twelve times longer than that for WE54-T6 (3.3h). At  $T=523\text{K}$  and  $\sigma=80\text{MPa}$ , the minimum creep rate of WGZ1152-T6 was almost one order of magnitude lower than that for WE54-T6. The minimum creep rate of WGZ1152-T6 was comparable to that for HZ32-T5 at  $T=573\text{K}$  and  $\sigma=30\text{MPa}$ .<sup>[18]</sup> From the slope, the creep stress exponent  $n$  can be determined as 4.5 for all the test temperatures.

Fig. 5 illustrates a representative creep curve at  $T=598\text{K}$  and  $\sigma=80\text{MPa}$  showing the primary stage strain  $\varepsilon_I$ , the secondary stage strain  $\varepsilon_{II}$ , and the tertiary stage strain  $\varepsilon_{III}$ . The secondary stage strain  $\varepsilon_{II}$  was determined by the following equation<sup>[19]</sup>

$$\varepsilon_{II} = t_r \cdot \dot{\varepsilon}_{\min}, \quad (1)$$

where  $\dot{\varepsilon}_{\min}$  is the minimum creep rate (minimum slope of creep curve). The primary stage strain  $\varepsilon_I$  was determined by the intersection of the tangent at the minimum slope of the creep curve with the creep strain axis at  $t=0$ .<sup>[14,19]</sup> The tertiary stage strain  $\varepsilon_{III}$  was determined by the following



equation<sup>[19]</sup>

$$\varepsilon_{\text{III}} = \varepsilon_{\text{r}} - \varepsilon_{\text{I}} - \varepsilon_{\text{II}}, \quad (2)$$

where  $\varepsilon_{\text{r}}$  is rupture strain (total creep strain). The stress dependence of the primary stage strain  $\varepsilon_{\text{I}}$ , the secondary stage strain  $\varepsilon_{\text{II}}$ , the tertiary stage strain  $\varepsilon_{\text{III}}$ , and the relative strain per creep stage  $\varepsilon_i/\varepsilon_{\text{r}}$  ( $i = \text{I, II, III}$ ) are illustrated in Fig. 6. At 573K [Fig. 6(a)], there was no clear tendency of the primary stage strain  $\varepsilon_{\text{I}}$ , the secondary stage strain  $\varepsilon_{\text{II}}$ , and the tertiary stage strain  $\varepsilon_{\text{III}}$  to stress. The average primary stage strain  $\varepsilon_{\text{I}}$  was  $0.17 \pm 0.04\%$ , and the average relative value of  $\varepsilon_{\text{I}}/\varepsilon_{\text{r}}$  was  $0.055 \pm 0.03$ . Except for  $\sigma=50\text{MPa}$ , the secondary stage strain  $\varepsilon_{\text{II}}$  was greater than the tertiary stage strain  $\varepsilon_{\text{III}}$ , with average  $\varepsilon_{\text{II}}/\varepsilon_{\text{r}}$  and  $\varepsilon_{\text{III}}/\varepsilon_{\text{r}}$  values of 0.58 and 0.37, respectively. For  $\sigma=50\text{MPa}$ , the  $\varepsilon_{\text{II}}/\varepsilon_{\text{r}}$  and  $\varepsilon_{\text{III}}/\varepsilon_{\text{r}}$  values were 0.24 and 0.73, respectively. At 598K [Fig. 6(b)], the primary stage strain  $\varepsilon_{\text{I}}$  was not sensitive to stress. The secondary stage strain  $\varepsilon_{\text{II}}$  and the tertiary stage strain  $\varepsilon_{\text{III}}$  increased with increasing stress. The values of  $\varepsilon_{\text{I}}/\varepsilon_{\text{r}}$ ,  $\varepsilon_{\text{II}}/\varepsilon_{\text{r}}$  and  $\varepsilon_{\text{III}}/\varepsilon_{\text{r}}$  were relatively insensitive to stress and were  $0.009 \pm 0.008$ ,  $0.32 \pm 0.018$  and  $0.67 \pm 0.009$ , respectively. The longer the tertiary creep life, the higher the  $\varepsilon_{\text{III}}/\varepsilon_{\text{r}}$  value was. This is consistent with Fig. 1-3, where the extended tertiary creep stage lasted longer at high temperatures and lower stresses.

The Arrhenius plot of the natural logarithm of the minimum creep rate versus the reciprocal of temperature at stresses between 50MPa to 140MPa is illustrated in Fig. 7. The activation energy for creep was determined from the slope. The activation energy for creep was independent of stress within the experimental deviation except for the highest stress of 140MPa (Fig. 8), where the activation energy for creep was 256kJ/mol. The average activation energy for creep,  $Q_{\text{avg}}$ , was  $221 \pm 20\text{kJ/mol}$  for all the studied stress levels.

### 3.2 Creep rupture

The creep damage tolerance parameter  $\lambda$  measures the tolerance of the material to strain concentrations, and is given by the following equation<sup>[20]</sup>

$$\lambda = \frac{\varepsilon_r}{\dot{\varepsilon}_{\min} \cdot t_r} \quad (3)$$

The plot of  $\varepsilon_r$  versus  $\dot{\varepsilon}_{\min} \cdot t_r$  is illustrated in Fig. 9, and the creep damage tolerance parameter,  $\lambda$ , could be determined from the slope. Note that the data of MRI153<sup>[5]</sup> [Mg-9Al-0.7Zn-1Ca-0.1Sr (wt.%) ] and WE54-T6 were also included for comparison, which will be discussed latter. The  $\lambda$  values of the studied WGZ1152-T6 alloy ranged from 1.4 to 2.5 for most test conditions. Only a few test conditions, such as T=573K/ $\sigma$ =50MPa and T=598K/ $\sigma$ =120MPa, exhibited a higher  $\lambda$  value ( $\lambda$ =3.2). The  $\lambda$  value was greater at higher temperatures and the bigger the  $\lambda$  value, the larger  $\varepsilon_{III}/\varepsilon_r$  was. This means that the proportion of the tertiary creep strain with respect to the overall creep strain is greater with increasing  $\lambda$ . A similar trend has been found in steels.<sup>[14]</sup>

Fig. 10 illustrates the creep rupture properties. For 573K, the rupture strain was not sensitive to the stress and roughly constant [Fig. 10 (a)]. For 598K, the rupture strain was increased with increasing stress [Fig. 10 (a)]. The rupture time decreased with increasing stress at all tested temperatures [Fig. 10 (b)]. Under intergranular creep fracture conditions, it is often observed that the minimum creep rate and the rupture time for many metals and alloys can be related by the Monkman-Grant (MGR) equation:<sup>[21-23]</sup>

$$\dot{\varepsilon}_{\min} t_r^m = C \quad (4)$$

Where m, and C are constants for a given material. The data for many materials is better fit by the modified Monkman-Grant relationship (MMGR):<sup>[24]</sup>

$$\frac{t_r \cdot \dot{\varepsilon}_{\min}^m}{\varepsilon_r} = C' \quad (5)$$

Where m' is close to unity and C' is independent of temperature and stress. The linear relationship

of minimum creep rate and time to rupture in log-log coordinates shows the Monkman-Grant relationship (MGR) according to Eq. (4) (Fig. 11). The values of  $m$  and  $C$  were 0.85 and 0.22, respectively. The linear relationship of  $\dot{\epsilon}_r/t_r$  versus minimum creep rate in log-log coordinates shows the modified Monkman-Grant relationship (MMGR) according to Eq. (5) (Fig. 12). The values of  $m'$  and  $C'$  were 1.04 and 0.26, respectively. It should be noted that the adjusted R square for the linear fit increased from 0.9480 to 0.9912 by using modified Monkman-Grant relationship, suggesting that the modified Monkman-Grant relationship provided a better fit for the studied alloy.

### 3.3 Initial microstructure

The peak-aged WGZ1152 microstructure has been described previously.<sup>[8,9]</sup> Fig. 13 illustrates a representative optical photomicrograph of the peak-aged microstructure. The average grain size was  $116 \pm 15 \mu\text{m}$ .<sup>[9]</sup> The strip-shaped  $\text{Mg}_{12}\text{YZn}$  phases were distributed along the grain boundaries, and the cuboid-shaped phases were present at both the grain boundaries and inside the grains. The measured mean diameter and volume fraction of the  $\text{Mg}_{12}\text{YZn}$  phase were  $7.2 \pm 4.9 \mu\text{m}$  and  $16.1 \pm 2.7\%$ , respectively.<sup>[9]</sup> For the cuboid-shaped phase the mean diameter and volume fraction were  $3.7 \pm 2.6 \mu\text{m}$  and  $2.1 \pm 0.3\%$ , respectively.<sup>[9]</sup> Fig. 14 shows a bright field TEM image and SADP of the  $\beta'$  precipitates, which provide strengthening.<sup>[9]</sup> Its structure was identified as an orthorhombic (bco,  $a=2 \times a_{\text{Mg}}=0.640\text{nm}$ ,  $b=8 \times d_{\text{Mg}}=2.223\text{nm}$ ,  $c=c_{\text{Mg}}=0.521\text{nm}$ ), and the composition was rich in rare earth elements.<sup>[9,25,26]</sup> As seen in the image, the fine spheroidal  $\beta'$  precipitates, whose diameter ranged between 5-40nm, were evenly dispersed in the matrix.

### 3.4 Microstructural evolution during creep exposure

Fig. 15 illustrates optical photomicrographs of the surface of specimens creep tested at  $T=598\text{K}$  and  $\sigma=50\text{MPa}$ , illustrating the microstructural evolution during the creep exposure. In the primary creep regime [stage I ( $t=0.5\text{h}$ ,  $\epsilon=0.10\%$ ), Fig.15 (a)], there were no detected changes compared to the initial microstructure. In the secondary creep regime [stage II ( $t=5\text{h}$ ,  $\epsilon=0.45\%$ )],

some short wavy slip traces, usually associated with non-basal slip and cross slip, were observed [Fig. 15(b), marked with white arrows], and some microcracks were present near grain boundary areas [Fig. 15(b) and (c), marked with black arrows]. In the tertiary creep regime [stage III ( $t=50\text{h}$ ,  $\varepsilon=6.2\%$ ), Fig.15 (d)], cross slip was evident (marked with white arrows), which again suggested that non-basal slip was active. The number of slip traces increased with increasing creep time and strain. At  $T=573\text{K}$  and  $\sigma=50\text{MPa}$ , there were no observed changes in the initial microstructure in the primary creep regime [stage I ( $t=5\text{h}$ ,  $\varepsilon=0.05\%$ ), Fig.16 (a)]. In the secondary creep regime [stage II ( $t=90\text{h}$ ,  $\varepsilon=0.42\%$ )], some long straight slip lines, normally associated with basal slip for Mg alloy, were observed [Fig. 16(b), marked with white arrows]. And this will be confirmed by the slip trace analysis which will be presented latter. Some microcracks were present near grain boundaries [Fig. 16(c), marked with black arrows]. This was similar to the secondary creep regime observations of the sample, which was creep tested at  $T=598\text{K}$  and  $\sigma=50\text{MPa}$  [Fig. 15(c)]. At  $T=523\text{K}$  and  $\sigma=50\text{MPa}$ , extensive linear slip traces were observed [Fig. 16(d), marked with white arrows] in the secondary creep regime [stage II, ( $t=380\text{h}$ ,  $\varepsilon=0.19\%$ )]. This suggested basal slip was active and predominant. This was similar to that observed at  $T=573\text{K}$  and  $\sigma=50\text{MPa}$  in the secondary creep regime [Fig. 16(b)]. Fig. 17 illustrates the microcracks observed in the secondary creep regime using SEM. The microcracks initiated at grain boundaries and propagated into the grain interior. Their length ranged from 1 to  $5\mu\text{m}$ .

Fig. 18 illustrates precipitates and cavities after creep exposure at  $573\text{K}$ . Dense coarse precipitates formed during the creep exposure, and the morphology of the precipitates was dependent on the creep testing condition. After  $4.8\text{h}$  of creep exposure at  $T=573\text{K}$  and  $\sigma=120\text{MPa}$  [Fig. 18(a)], the spheroid precipitates (average size  $0.1\text{-}0.5\mu\text{m}$ ) dominated, as seen in the insert in Fig. 18(a). After  $85\text{h}$  of creep exposure at  $T=573\text{K}$  and  $\sigma=70\text{MPa}$  [Fig. 18(b)], the spheroid

precipitates were still present and some plate-shaped precipitates formed. After 676h of creep exposure at  $T=573\text{K}$  and  $\sigma=50\text{MPa}$  [Fig. 18(c)], the volume of the plate-shaped precipitates, with an average length between  $5\text{-}20\mu\text{m}$ , increased significantly. It should be noted that the plate-shaped precipitates were relatively stable and did not transform or coarsen during the 676h to 1114h creep exposure [Fig. 18 (c) and (d)]. Fig. 19 (a) and (b) illustrate TEM bright field images and SADPs of the dominant precipitates in the specimens after 41h and 676h of creep exposure, respectively. Taking into account the four-staged precipitation sequence:<sup>[25,27]</sup>  $\alpha\text{-Mg}$  Solid solution  $\rightarrow \beta''$  ( $\text{D}_{019}$ )  $\rightarrow \beta'$  ( $\text{bco}$ )  $\rightarrow \beta_1$  ( $\text{fcc}$ )  $\rightarrow \beta$  ( $\text{fcc}$ ) in the Mg-RE alloys as well as the corresponding SADPs (Fig. 19), it is likely that the spheroid precipitate was the metastable  $\beta'$  phase and the plate-shaped precipitate was the equilibrium  $\beta$  phase. Therefore, it is suggested that the dominant  $\beta'$  phase transformed to the  $\beta$  phase with increasing creep time. It should be noted that the  $\beta'$  phase coarsened considerably after creep exposure compared to the undeformed condition. Besides the dense precipitates which formed during the creep exposure, another characteristic of the crept microstructure was creep cavitation (Fig. 18). The creep cavities preferentially nucleated at grain boundaries and the interface between the Mg matrix and the secondary phase ( $\text{Mg}_{12}\text{YZn}$ ). Some isolated cavities coalesced and formed continuous intergranular cracks, as seen in the insert in Fig. 18(b). The precipitate-free zones, with a width of approximately  $2.5\mu\text{m}$ , adjacent to the grain boundaries are illustrated in Fig. 18(b).

The deformation evolution during an *in-situ* creep test at  $T=573\text{K}$  and  $\sigma=50\text{MPa}$  is shown in Fig. 20. In the primary creep regime [stage I, Fig. 20(a)], only one grain exhibited slip bands in the area observed (marked with white arrow). More slip bands were present, not only in the same grain but also in some other grains, with increasing creep time [stage II and III, Fig. 20(b) and (c), respectively]. This is similar with the previous surface observations in the conventional creep tests

[Fig. 15(b) and (d)]. The slip traces were long and straight, which is consistent with the *ex-situ* surface observations in the conventional creep tests in the same creep condition [Fig. 16(b)]. The active slip systems were identified using the EBSD data and the SE SEM images acquired after the *in-situ* creep test. Based on the literatures,<sup>[28-30]</sup> three slip modes were used for deformation analysis: basal  $\langle a \rangle$  ( $\{0001\}\langle -2110 \rangle$ ), first-order prismatic  $\langle a \rangle$  ( $\{01-10\}\langle 2-1-10 \rangle$ ), and second-order pyramidal  $\langle c+a \rangle$  ( $\{11-22\}\langle -1-123 \rangle$ ). Fig. 21 illustrates the slip trace methodology used to identify the active slip systems from the SE SEM images and the EBSD orientation data using a MATLAB code with the inputs of grain Euler angles and all available slip systems. The active slip systems were investigated in 90 grains, and only one set of slip traces was observed for one grain. Fig. 22 summarizes the Schmid factor distributions and the number of identified slip systems. Among the 90 slip trace analyzed, 90% (81) were basal  $\langle a \rangle$  slip, 7.8% (7) were pyramidal  $\langle c+a \rangle$  slip, and 2.2% (2) were prismatic  $\langle a \rangle$  slip. This was confirmed that the basal slip was dominated, and non-basal slip was activated at  $T=573\text{K}$ . It was reasonable to believe that the similar long and straight slip traces, which were observed in the conventional creep tests at the same temperature of 573K [Fig. 16(b)] and the lower temperature of 523K [Fig. 16(d)], suggested the basal slip was active and predominant. Fig. 23 illustrates the intergranular crack initiation and propagation during the *in-situ* creep test in the same creep condition. No obvious cracking was observed in the secondary creep regime [stage II, Fig. 23(a)]. The boundaries marked with white arrows cracked during the tertiary creep regime [stage III, Fig. 23(b)-(d)]. Cracking initiated preferentially at grain boundaries and near the  $\text{Mg}_{12}\text{YZn}$  phases located at grain boundaries, and the crack propagation path tended to follow the grain boundaries. With increased creep time, the intergranular cracks grew in length and width. Fig. 24 illustrates the edge crack evolution, which caused the final rupture. Several macro-edge cracks marked with white arrows were observed in the late stage of tertiary creep [Fig. 24(a)]. One of them was relatively large and propagated

rapidly, and caused the final rupture (see solid arrow in Fig. 24). Fig. 24(c) illustrates the primary crack at higher magnification, showing its propagation path along the grain boundaries. Secondary cracks were marked with dash arrows. More secondary cracks were present with increasing creep time and displacement [Fig. 24(a) and (b)]. Fig. 25 illustrates backscatter electron SEM photomicrograph representing a grain boundary cracking in the subsurface bulk microstructure of an *in-situ* creep tested specimen at  $T=573\text{K}$  and  $\sigma=50\text{MPa}$ . The surface *in-situ* observations agreed with the bulk *ex-situ* observations, however the extent of the cracking appeared to be slightly less within the bulk compared to the surface.

## 4. Discussion

### 4.1 Extended tertiary creep

The primary, secondary and tertiary creep regimes are well defined for pure metals and single phase alloys.<sup>[31]</sup> The secondary creep stage is a period of nearly constant minimum creep rate, where a balance between the competing processes of strain hardening and recovery occurs.<sup>[32]</sup> However, for WGZ1152, the tertiary creep stage dominates and occupies most of the creep life. Similar creep behavior has been found in many different kinds of complex engineering alloys, such as Ni-Cr-base superalloys which are currently used as blades in gas turbines.<sup>[15,33]</sup> Other alloys that exhibit this behavior are 316L austenitic steel,<sup>[14]</sup> 1Cr-1Mo-0.25V bainitic steel,<sup>[14]</sup> 0.5Cr-0.5Mo-0.25V ferritic steel,<sup>[34]</sup> Mg-Al-Ca alloy<sup>[5]</sup> and AZ91hp<sup>[35]</sup>. Normal tertiary creep occurs when there is an effective reduction in cross-sectional area either because of necking or internal void formation, such as grain boundary cavitation and cracking.<sup>[32]</sup> The extended tertiary creep is generally believed to be a consequence of precipitate coarsening<sup>[5,34-36]</sup> or strain-induced instability of the dislocation substructure<sup>[15,33]</sup>. As described in the previous section, the fine  $\beta'$  phase, of diameter between 5-40nm in the initial condition (Fig. 14), coarsened to 0.1-0.5 $\mu\text{m}$  after 4.8h of creep exposure [Fig. 18(a)], and the plate-shaped  $\beta$  precipitates, with an average length of

5-20 $\mu\text{m}$ , formed during the 676h creep exposure [Fig. 18(c)]. It is reasonable to believe that the extended tertiary creep observed in this study is associated with precipitate coarsening. This rationale is strengthened by the observation that the precipitates coarsen significantly at high temperature and low stress.

## 4.2 Creep deformation mechanisms

At elevated temperatures, the minimum creep rate ( $\dot{\epsilon}_{\text{min}}$ ) of many metals and alloys is generally described by the following equation:<sup>[7,31,32,37,38]</sup>

$$\dot{\epsilon}_{\text{min}} = A\sigma^n \exp\left(-\frac{Q}{RT}\right) \quad (6)$$

Where A is a material constant,  $\sigma$  is the stress, n is the stress exponent, Q is the activation energy for creep, R is the gas constant and T is the absolute temperature. A useful method of obtaining a guide to the creep deformation mechanism is to determine the stress exponent n and the activation energy Q for creep based on Eq. (6).

As seen in Fig. 4, the n was independent of temperature, and its value was 4.5 implying that dislocation creep was the rate-controlling mechanism.<sup>[31,32]</sup> An n value of approximately 5 is commonly observed for Mg and Mg alloys, such as pure Mg,<sup>[37,39]</sup> Mg-Al-based alloys,<sup>[38,40-42]</sup> Mg-Zn-based alloys,<sup>[43,44]</sup> Mg-Sm-based alloys<sup>[45-47]</sup> and Mg-Y-based alloys<sup>[6,48,49]</sup>. The measured  $Q_{\text{avg}}$  value of  $221 \pm 20\text{kJ/mol}$  was much higher than the activation energy for lattice self-diffusion,  $Q_{\text{sd}}$ , of Mg (135kJ/mol).<sup>[50]</sup> High activation energy values for creep have also been found in pure Mg,<sup>[37]</sup> Mg-0.8%Al solid solution alloy,<sup>[38]</sup> Mg-5Al-1Sr,<sup>[41]</sup> Mg-Sc based alloys,<sup>[18]</sup> and Mg-Y based alloys<sup>[6,49]</sup>. Vagarali *et al*<sup>[37]</sup> reported the activation energy for creep in pure Mg to be  $220 \pm 10\text{kJ/mol}$  in the temperature range 600-750K, and there was evidence of extensive non-basal slip. They concluded this behavior was consistent with cross slip from basal to prismatic planes. Suzuki *et al*<sup>[51]</sup> studied the creep behavior of binary Mg-Y alloys at 550-650K, and found the activation energy for creep was 230-290kJ/mol depending on the Y content. Furthermore, a



transition from basal slip at 550K to non-basal slip at 650K was revealed by TEM.<sup>[51]</sup> Suzuki *et al*<sup>[51]</sup> believed that the cross slip was responsible for high activation energy value for creep. In the present study, the measured  $Q_{avg}$  was close to those mentioned above. The slip traces analysis confirmed the non-basal slip was activated (10%) at 573K (Fig. 21 and 22), and the surface creep deformation observations suggested that non-basal slip and cross slip were active and prevalent at  $T=598K$  [Fig.15 (d)]. Thus, it is reasonable to believe that the measured high activation energy for creep is associated with the activation of non-basal slip and cross slip. Another microstructural feature which may have contributed to the high activation energy for creep was the second-phase particles, especially those present at the grain boundaries.<sup>[5,41,52,53]</sup> These particles can act as effective obstacles to matrix dislocation motion both within the grains and at the grain boundaries. The dislocations may pile up. According to the model developed by Dunand and Jansenet,<sup>[53,54]</sup> with increasing temperature the number of the pile-up dislocations decreased by climbing due to the increased jog nucleation rate and dislocation climb velocity, leading to a stronger temperature dependence of the threshold stress and a higher measured activation energy for creep. Thus, the  $\beta'$  and  $\beta$  precipitates dispersed in the matrix as well as the thermally stable  $Mg_{12}YZn$ <sup>[9]</sup> at grain boundaries may have combined to contribute to the high activation energy for creep.

### 4.3 Creep rupture mechanisms

The creep damage tolerance parameter  $\lambda$  is an important parameter in assessing the susceptibility of a material to localized cracking where strain concentrations exist,<sup>[15]</sup> and it may also be used to help identify the damage mechanisms for tertiary creep and final rupture.<sup>[55]</sup> The value of  $\lambda$  for engineering alloys ranges from 1 to 20.<sup>[20]</sup> From Eq. (3), it is evident that when  $\lambda=1$ , fracture occurs as soon as a small amount of damage has occurred and the material is brittle. With higher values of  $\lambda$ , the material may endure a larger amount of damage before it fails.<sup>[20]</sup> Theoretical calculation has predicted that when  $\lambda$  ranges from about 1-2.5, grain-boundary cavities

and cracks attribute significantly to tertiary creep and final rupture.<sup>[55]</sup> In the present study, the  $\lambda$  values ranged between 1.4 and 2.5, which implies that grain boundary cavities and cracks may play an important role in the creep rupture. The *in-situ* observations confirmed that grain boundary cavities were present in the tertiary creep stage. As shown in Fig. 9, the creep damage tolerance parameter  $\lambda$  and creep rupture strain of the studied alloy were compared with that for a MRI153<sup>[5]</sup> and WE54-T6. MRI153 was a newly developed creep-resistant Mg alloy for powertrain applications with complicated geometries such as automatic transmission cases, oil pans, valve covers, and intake manifolds.<sup>[5,56]</sup> For instance, it has been demonstrated and confirmed by trials of automatic transmission cases for Polo, Passat, Audi 3, Audi TT, and Audi 6.<sup>[56]</sup> WE54 is the most commercially used creep-resistant Mg alloy. It has been used for high performance automotive applications such as F1 and Indy car engine and gearbox components.<sup>[17]</sup> The  $\lambda$  values of the MRI153 ranged from 1.5 to 2.3 for most tested conditions.<sup>[5]</sup> These values lay in the similar range of the studied alloy. Actually, for a few conditions, the  $\lambda$  values of the studied alloy ( $\lambda=3.2$ ) were higher than that for the MRI153. The rupture strain of the MRI153 ranged from 5-6% and 7-10% at  $T=423\text{K}$  and  $T=473\text{K}$ , respectively.<sup>[5]</sup> These values are comparable to those for the studied alloy, which were from 2-5% at  $T=523\text{-}573\text{K}$  and 11-17% at  $T=598\text{K}$ . For WE54-T6, the  $\lambda$  values were about 4.5, and the rupture strain ranged from 7-19%. These values were higher, but not very much, than those for the studied alloy. Although these comparisons are based on different test conditions, they are still useful for evaluating the practical applicability of the studied alloy because that all these test conditions were chosen based on the potential applications of each alloy. All in all, although the studied alloy exhibited low creep rupture strain and low creep damage tolerance parameter, it may be used for the applications which do not require high creep ductility such as engine piston applications.<sup>[10]</sup> A comprehensive and strict estimate of

this issue considering more specific applications is needed and will be the next work before the studied alloy comes into its practice use.

The minimum creep rate and rupture time could be described by the original and modified Monkman-Grant relationships for the WGZ1152-T6 alloy. For the Monkman-Grant relationship, the  $m$  and  $C$  were 0.85 and 0.22, respectively. These values lie in the range 0.8-0.95 and 0.05-0.5, respectively, reported for most of metals and alloys.<sup>[19,21]</sup> For the modified Monkman-Grant relationship, the  $m'$  value (1.04) was close to 1 indicating that the  $\dot{\epsilon}_r/t_r$  was proportional to the minimum creep rate. The  $C'$  value (0.26) was in the range 0.1-0.79 reported for many metals and alloys.<sup>[19,21,57]</sup> The Monkman-Grant relationship can be useful for both engineering application as well as scientific understanding.<sup>[19]</sup> For example, using the constants  $C$  and  $m$ , and the minimum creep rate, one can estimate the rupture time. In terms of its scientific aspect, the Monkman-Grant relationship can be useful for understanding the creep-rupture mechanisms. Although the Monkman-Grant relationship is proposed as an empirical relationship,<sup>[23]</sup> many researchers have attempted to rationalize it on the basis of intergranular creep rupture models which presume the rupture time to be controlled largely by the growth of the isolated cavities at the grain boundaries.<sup>[19,21,22]</sup>

The good agreement of the data with the original and modified Monkman-Grant relationships as well as the calculated creep damage tolerance parameter  $\lambda$  values are consistent with the microstructural observations of the creep deformation, which revealed the intergranular cracking was the dominant fracture mode. The microcracks (Fig. 17) and cavities (Fig. 18) preferentially nucleated at grain boundaries and the interface between Mg matrix and the secondary phase ( $Mg_{12}YZn$ ). The accumulation and growth of such microcracks and cavities can lead to their joining and subsequent continuous intergranular cracking. The cavities usually nucleate at grain boundaries and the interface between the matrix and secondary phases. This is because that these

locations can generate sufficient stress concentration for the nucleation and growth of cavities<sup>[58]</sup>

The observed precipitate-free zones adjacent to grain boundaries [Fig. 18(b)], which are intrinsically weak regions (where no precipitation hardening and solid solution strengthening occur), may also aid to the intergranular cracking.

## 5. Conclusions

The creep and rupture behavior of peak-aged Mg-11Y-5Gd-2Zn-0.5Zr (wt.%) (WGZ1152) at temperatures between 523-598K (0.58-0.66 $T_m$ ) and stresses between 30MPa to 140MPa were investigated. The main conclusions of this work are summarized below:

(1) The newly developed WGZ1152 alloy exhibited potential for creep-resistant applications at temperatures up to 598K. The minimum creep rate is significantly lower than that for the WE54-T6 alloy at  $T=523-573K$  (0.58-0.64 $T_m$ ) and  $\sigma=50-80MPa$ , and is comparable to the HZ32-T5 at  $T=573K$  and  $\sigma=30MPa$ .

(2) WGZ1152 exhibited an extended tertiary creep stage, which is believed to be associated with the  $\beta'$  and  $\beta$  precipitate coarsening during the creep exposure. The greater the tertiary creep life, the higher the ratio between the tertiary creep strain and the rupture strain ( $\epsilon_{III}/\epsilon_r$ ) was.

(3) For all test temperatures, the creep exponent value was 4.5 implying that dislocation creep was the rate-controlling mechanism. The average activation energy  $Q_{avg}$  value of  $221 \pm 20kJ/mol$  was higher than that for lattice self-diffusion of Mg (135kJ/mol). This was considered to be associated with the activation of non-basal slip and cross slip. This was consistent with the surface deformation observations, which suggested that a transition from basal slip to non-basal slip and cross slip occurred with increasing temperature.

(4) The minimum creep rate and rupture time can be well described by the original and modified Monkman-Grant relationships. The microcracks and cavities preferentially nucleated at grain boundaries and the interface between the Mg matrix and the secondary phase. Intergranular

cracking was the dominant creep fracture mode. This is consistent with the creep damage tolerance parameter range of 1.3-2.5.

## Acknowledgement

This work was supported by the National Natural Science Foundation of China (NO. 51074106), Key Hi-Tech Research and Development Program of China (2009AA033501), National Key Technology R & D Program of China (2011BAE22B01-5) and International Cooperation Fund of Shanghai Science and Technology Committee, Shanghai/Rhone-Alpes Science and Technology cooperation fund (No.06SR07104).

## References:

- [1] B. L. Mordike and K. U. Kainer, *Magnesium Alloys and Their Applications*, Wiley, New York, 2000, p. 816.
- [2] A. Luo and M. O. Pekguleryuz: *J. Mater. Sci.*, 1994, vol. 29, pp. 5259-5271.
- [3] B. L. Mordike and T. Ebert: *Mat. Sci. Eng. A*, 2001, vol. 302, pp. 37-45.
- [4] A. A. Luo: *Int. Mater. Rev.*, 2004, vol. 49, pp. 13-30.
- [5] S. Zhu, J. Nie and B. Mordike: *Metall. Mater. Trans. A*, 2006, vol. 37, pp. 1221-1229.
- [6] B. L. Mordike: *Mat. Sci. Eng. A*, 2002, vol. 324, pp. 103-112.
- [7] M. Pekguleryuz and M. Celikin: *Int. Mater. Rev.*, 2010, vol. 55, pp. 197-217.
- [8] Y. Gao, Q. D. Wang, J. H. Gu, Y. Zhao, Y. Tong and D. D. Yin: *J. Alloy. Compd*, 2009, vol. 477, pp. 374-378.
- [9] D. D. Yin, Q. D. Wang, Y. Gao, C. J. Chen and J. Zheng: *J. Alloy. Compd*, 2011, vol. 509, pp. 1696-1704.
- [10] K. Okamoto, M. Sasaki, N. Takahashi, Q. D. Wang, Y. Gao, D. D. Yin and C. J. Chen, *Applicability of Mg-Zn-(Y, Gd) Alloys for Engine Pistons*, in: *Magnesium Technology 2011*, 2011.
- [11] C. J. Chen, Q. D. Wang and D. D. Yin: *J. Alloy. Compd*, 2009, vol. 487, pp. 560-563.
- [12] C. J. Boehlert, C. J. Cowen, S. Tamirisakandala, D. J. Mceldowney and D. B. Miracle: *Scripta Mater.*, 2006, vol. 55, pp. 465-468.
- [13] J. P. Quast and C. J. Boehlert: *Metall. Mater. Trans. A*, 2007, vol. 38, pp. 529-536.
- [14] B. Wilshire and H. Burt: *Int. J. Pres. Ves. Pip.*, 2008, vol. 85, pp. 47-54.
- [15] B. F. Dyson and T. B. Gibbons: *Acta Mater.*, 1987, vol. 35, pp. 2355-2369.
- [16] W. Blum, Y. Li, X. Zeng, P. Zhang, B. von Großmann and C. Haberling: *Metall. Mater. Trans. A*, 2005, vol. 36, pp. 1721-1728.
- [17] J. F. King, *Development of Practical High Temperature Magnesium Casting Alloys*, in: *Magnesium Alloys and Their Applications*, Wiley, New York, 2000, pp. 14-22.
- [18] B. Mordike, I. Stulíková and B. Smola: *Metall. Mater. Trans. A*, 2005, vol. 36, pp. 1729-1736.
- [19] D. C. Dunand, B. Q. Han and A. M. Jansen: *Metall. Mater. Trans. A*, 1999, vol. 30, pp. 829-838.
- [20] D. P. Miannay, *Time-dependent fracture mechanics*, Springer, New York, 2001, p. 313.
- [21] G. Sundararajan: *Mat. Sci. Eng. A*, 1989, vol. 112, pp. 205-214.
- [22] F. Povolo: *J. Mater. Sci.*, 1985, vol. 20, pp. 2005-2010.

- [23] F. C. Monkman and N. J. Grant: Proc. ASTM., 1956, vol. 56, pp. 593-620.
- [24] F. Dobes and K. Milicka: Met. Sci., 1976, vol. 10, pp. 382-384.
- [25] J. F. Nie and B. Muddle: Acta Mater., 2000, vol. 48, pp. 1691-1703.
- [26] T. Honma, T. Ohkubo, S. Kamado and K. Hono: Acta Mater., 2007, vol. 55, pp. 4137-4150.
- [27] S. M. He, X. Q. Zeng, L. M. Peng, X. Gao, J. F. Nie and W. J. Ding: J. Alloy. Compd, 2006, vol. 421, pp. 309-313.
- [28] M. Barnett: Metall. Mater. Trans. A, 2003, vol. 34, pp. 1799-1806.
- [29] J. Koike, T. Kobayashi, T. Mukai, H. Watanabe, M. Suzuki, K. Maruyama and K. Higashi: Acta Mater., 2003, vol. 51, pp. 2055-2065.
- [30] Z. Keshavarz and M. R. Barnett: Scripta Mater., 2006, vol. 55, pp. 915-918.
- [31] M. E. Kassner and M. T. Perez-Prado: Prog. Mater. Sci., 2000, vol. 45, pp. 1-102.
- [32] G. E. Dieter, Mechanical metallurgy, McGraw-Hill, New York, 1986, p. 751.
- [33] B. F. Dyson and M. McLean: Acta Mater., 1983, vol. 31, pp. 17-27.
- [34] K. R. Williams and B. Wilshire: Mat. Sci. Eng., 1977, vol. 28, pp. 289-296.
- [35] P. Zhang, B. Watzinger and W. Blum: phys. stat. sol. (a), 1999, vol. 175, pp. 481-489.
- [36] R. A. Stevens and P. E. J. Flewitt: Acta Mater., 1981, vol. 29, pp. 867-882.
- [37] S. S. Vagarali and T. G. Langdon: Acta Mater., 1981, vol. 29, pp. 1969-1982.
- [38] S. S. Vagarali and T. G. Langdon: Acta Mater., 1982, vol. 30, pp. 1157-1170.
- [39] R. B. Jones and J. E. Harris: ARCHIVE: Proceedings of the Institution of Mechanical Engineers, Conference Proceedings 1964-1970 (vols 178-184), Various titles labelled Volumes A to S, 1963, vol. 178, pp. 1-8.
- [40] M. Regev, E. Aghion, S. Berger, M. Bamberger and A. Rosen: Mat. Sci. Eng. A, 1998, vol. 257, pp. 349-352.
- [41] P. Zhao, Q. Wang, C. Zhai and Y. Zhu: Mat. Sci. Eng. A, 2007, vol. 444, pp. 318-326.
- [42] Z. Chen, J. Huang, R. F. Decker, S. E. Lebeau, L. R. Walker, O. B. Cavin, T. R. Watkins and C. J. Boehlert: Metall. Mater. Trans. A, 2011, vol. 42, pp. 1386-1399.
- [43] C. J. Boehlert and K. Knittel: Mat. Sci. Eng. A, 2006, vol. 417, pp. 315-321.
- [44] C. J. Boehlert: J. Mater. Sci., 2007, vol. 42, pp. 3675-3684.
- [45] J. Zheng, Q. D. Wang, Z. L. Jin and T. Peng: Mat. Sci. Eng. A, 2010, vol. 527, pp. 4605-4612.
- [46] J. Zheng, Q. D. Wang, Z. L. Jin and T. Peng: Mat. Sci. Eng. A, 2010, vol. 527, pp. 1677-1685.
- [47] J. Zheng, Q. D. Wang, Z. L. Jin and T. Peng: J. Alloy. Compd, 2010, vol. 496, pp. 351-356.
- [48] Q. D. Wang, D. Q. Li, J. J. Blandin and M. Suery: Mat. Sci. Eng. A, 2009, vol. 516, pp. 189-192.
- [49] J. G. Wang, L. M. Hsiung, T. G. Nieh and M. Mabuchi: Mat. Sci. Eng. A, 2001, vol. 315, pp. 81-88.
- [50] M. F. Ashby and H. J. Frost, Deformation-mechanism maps :the plasticity and creep of metals and ceramics, Pergamon Press, Oxford, 1982, p. 166.
- [51] M. Suzuki, H. Sato, K. Maruyama and H. Oikawa: Mat. Sci. Eng. A, 2001, vol. 319-321, pp. 751-755.
- [52] J. Cadec, Creep in Metallic Materials, Amsterdam, 1988.
- [53] A. M. Jansen and D. C. Dunand: Acta Mater., 1997, vol. 45, pp. 4583-4592.
- [54] D. C. Dunand and A. M. Jansen: Acta Mater., 1997, vol. 45, pp. 4569-4581.
- [55] M. F. Ashby and B. F. Dyson, Creep damage mechanics and micromechanisms, in: R. S. Valluri (Ed. Advances in fracture research, vol 1, Pergamon Press, Oxford and New York, 1984, pp. 3-30.
- [56] E. Aghion, B. Bronfin, F. Von Buch, S. Schumann and H. Friedrich: JOM, 2003, vol. 55, pp. A30-A33.
- [57] F. Hnilica, V. Janik, B. Smola, I. Stulikova and V. Ocenasek: Mat. Sci. Eng. A, 2008, vol. 489, pp. 93-98.
- [58] M. E. Kassner and T. A. Hayes: Int. J. Plasticity, 2003, vol. 19, pp. 1715-1748.

## List of Figures

Fig. 1. Creep rate curves of the WGZ1152-T6 at T=598K: (a) creep strain rate versus time; (b) creep strain rate versus creep strain. Note that the specimens which were creep tested to failure were indicated with “X”.

Fig. 2. Creep rate curves of the WGZ1152-T6 at T=573K: (a) creep strain rate versus time; (b) creep strain rate versus creep strain. Note that the specimens which were creep tested to failure were indicated with “X”.

Fig. 3. Creep rate curves of the WGZ1152-T6 at T=523K: (a) creep strain rate versus time; (b) creep strain rate versus creep strain. Note that the specimens which were creep tested to failure were indicated with “X”.

Fig. 4. Log-Log plot of the stress dependence on the minimum creep rate at T=523-598K. Note that the data of WE54-T6 and HZ32<sup>[5]</sup>-T5 were also presented for comparison.

Fig. 5. Representative creep curve of the WGZ1152-T6 at T=598K and  $\sigma=80\text{MPa}$  showing the primary stage strain  $\epsilon_I$ , the secondary stage strain  $\epsilon_{II}$  and the tertiary stage strain  $\epsilon_{III}$ , along with the creep strain rate as a function of time.

Fig. 6. Stress dependence of the primary stage strain  $\epsilon_I$ , the secondary stage strain  $\epsilon_{II}$ , the tertiary stage strain  $\epsilon_{III}$  and the relative strain per creep stage  $\epsilon_i/\epsilon_r$  ( $i = I, II, III$ ),  $\epsilon_r$ =total creep strain, at (a) 573K and (b) 598K. At 598K, the majority of the strain was archived in the tertiary creep stage.

Fig. 7. The Arrhenius plot of the natural logarithm of minimum creep rate versus the reciprocal of temperature at stresses between 50MPa to 140MPa.

Fig. 8. Activation energy Q for creep versus stress.

Fig. 9. Relationship between rupture strain  $\varepsilon_r$  and  $\dot{\varepsilon}_{\min} \cdot t_r$ , where  $t_r$ =rupture time, showing the creep damage tolerance parameter  $\lambda$ . Note that the data of MRI153<sup>[5]</sup> and WE54-T6 were also presented for comparison.

Fig. 10. The stress dependence on (a) creep rupture strain and (b) creep rupture time at T=523-598K.

Fig. 11. Log-Log plot of minimum creep rate versus time-to-rupture at T=523-598K and stresses between 50MPa to 140MPa illustrating the Monkman-Grant relationship (MGR).

Fig. 12. Log-Log plot of  $\varepsilon_r/t_r$  versus minimum creep rate at T=523-598K and stresses between 50MPa to 140MPa illustrating the modified Monkman-Grant relationship (MMGR).

Fig. 13. Optical photomicrograph of the peak-aged WGZ1152-T6 microstructure.

Fig. 14. TEM bright field image and SADP of the fine  $\beta'$  precipitates in peak-aged WGZ1152-T6. The beam direction is approximately parallel to  $[0001]$  zone axis.

Fig. 15. Optical photomicrographs of the surface of specimens creep tested at T=598K and  $\sigma=50$ MPa illustrating microstructural evolution during creep exposure: (a) creep stage I (t=0.5h,  $\varepsilon=0.10\%$ ), (b) and (c) creep stage II (t=5h,  $\varepsilon=0.45\%$ ) and (d) creep stage III (t=50h,  $\varepsilon=6.2\%$ ). The tensile axis was horizontal.

Fig. 16. Optical photomicrographs of the surface of specimens creep tested at T=573K and  $\sigma=50$ MPa [(a)-(c)] illustrating microstructural evolution during creep exposure: (a) creep stage I (t=5h,  $\varepsilon=0.05\%$ ), (b) and (c) creep stage II (t=90h,  $\varepsilon=0.42\%$ ). (d) Creep tested at T=523K and  $\sigma=50$ MPa, creep stage II (t=380h,  $\varepsilon=0.19\%$ ). The tensile axis was horizontal.



Fig. 17. Secondary electron SEM photomicrographs of the surface of a specimen creep tested to stage II ( $t=90\text{h}$ ,  $\epsilon=0.42\%$ ) at  $T=573\text{K}$  and  $\sigma=50\text{MPa}$  showing microcracks near grain boundaries. The tensile axis was horizontal.

Fig. 18. Secondary electron SEM photomicrographs of creep tested specimens: (a)  $t=4.8\text{h}$ ,  $\epsilon=2.2\%$  ( $T=573\text{K}$  and  $\sigma=120\text{MPa}$ ), (b)  $t=85\text{h}$ ,  $\epsilon=2.5\%$  ( $T=573\text{K}$  and  $\sigma=70\text{MPa}$ ), (c)  $t=676\text{h}$ ,  $\epsilon=5.4\%$  ( $T=573\text{K}$  and  $\sigma=50\text{MPa}$ ) and (d)  $t=1114\text{h}$ ,  $\epsilon=1.2\%$  ( $T=573\text{K}$  and  $\sigma=30\text{MPa}$ ).

Fig. 19. TEM bright field images and SADPs of creep tested specimens with different creep time, showing (a) coarsened  $\beta'$  precipitates,  $t=41\text{h}$ ,  $\epsilon=3.0\%$  ( $T=573\text{K}$  and  $\sigma=80\text{MPa}$ ) and (b)  $\beta$  precipitates,  $t=676\text{h}$ ,  $\epsilon=5.4\%$  ( $T=573\text{K}$  and  $\sigma=50\text{MPa}$ ). The beam direction was approximately parallel to  $[0001]$  zone axis.

Fig. 20. Secondary electron SEM photomicrographs taken during an *in-situ* creep test at  $T=573\text{K}$  and  $\sigma=50\text{MPa}$ , where the number of surface slip traces (indicated with arrows) bands increased with increased creep time. The creep stages and displacements were indicated in the figures. The tensile axis was horizontal.

Fig. 21. Examples of the slip trace analysis performed to grain NO. 46 in (a), taken for the sample *in-situ* creep tested at  $T=573\text{K}$  and  $\sigma=50\text{MPa}$ . (a) the SE SEM photomicrograph, (b) EBSD orientation maps in ND, and (c) the slip system selection. Note that 2 was the selected system based on the match and this corresponds to the  $(0\ 0\ 0\ 1)$  plane and  $[-1\ 2\ -1\ 0]$  direction. The Schmid factors for the slip systems are indicated on the right hand side.

Fig. 22. The Schmid factor distributions and the number of identified slip systems for the sample *in-situ* creep tested at  $T=573\text{K}$  and  $\sigma=50\text{MPa}$ .

Fig. 23. Secondary electron SEM photomicrographs taken during an *in-situ* creep test at  $T=573\text{K}$  and  $\sigma=50\text{MPa}$  illustrating intergranular cracking initiation and propagation. The creep stages and displacements were indicated in the figures. The tensile axis was horizontal.

Fig. 24. Secondary electron SEM photomicrographs taken during an *in-situ* creep test at  $T=573\text{K}$  and  $\sigma=50\text{MPa}$  illustrating edge cracking initiation and propagation. The creep stages and displacements were indicated in the figures. The tensile axis was horizontal.

Fig. 25. Backscatter electron SEM photomicrograph represents a grain boundary cracking in the subsurface bulk microstructure of an *in-situ* creep tested specimen at  $T=573\text{K}$  and  $\sigma=50\text{MPa}$ . The tensile axis was horizontal.